RESULTS OF CONDUCOR TESTING IN SULTAN: A REVIEW*

R. Wesche#, M. Bagnasco, P. Bruzzone, M. Calvi, F. Cau, R. Herzog, C. Marinucci, B. Stepanov,
Ecole Polytechnique Fédérale de Lausanne, Centre de Recherches en Physique des Plasmas,
Association EURATOM-Confédération Suisse, 5232 Villigen PSI, Switzerland

Abstract

In the last few years, the DC performance of a large number of sub- and full-size NbTi as well as Nb_3Sn cable-in-conduit (CIC) conductors was tested in the SULTAN facility of CRPP. The "potential" DC performance of various CIC conductors was estimated from the measured strand data. In the present work, the DC performance of CIC conductors, measured in SULTAN, is compared with this "potential" DC performance. The DC performance of NbTi sub- and full size CIC conductors has been found to be in good agreement with the "potential" conductor performance. For Nb_3Sn CIC conductors, the situation is more complex because of the strain sensitivity of the critical current. Evidence for strand damage, caused by the large Lorentz forces, has been found in Nb_3Sn sub-size conductors. Finally, a summary of the results of the tests of the ITER-TF Nb_3Sn conductors is provided. Again the measured DC performance is compared to the "potential" performance.

INTRODUCTION

The unique SULTAN test facility [1] provides the possibility to measure the critical current of large cable-in-conduit (CIC) conductors of approximately 3.5 m length in background fields of up to 11 T. In a comparison of the measured CIC conductor critical current with the strand performance, the variation of the magnetic field within the conductor cross-section due to the self-field contribution needs to be taken into account. Moreover, a current imbalance originating from the resistance distribution in the joints may reduce the critical current. In the case of Nb_3Sn-based CIC conductors the strain state of the strands in the cable is not exactly known. Furthermore, Nb_3Sn is a brittle material, which is sensitive to micro-crack formation leading to an irreversible degradation of the current carrying capacity of the strands. For a single Nb_3Sn CIC conductor, it is therefore difficult to identify the reasons of unexpectedly low performance.

In order to get deeper insight in the relations between strand and conductor performances, the statistics of the results of the measurement of the critical current or the current sharing temperature in various NbTi and Nb_3Sn CIC sub- as well as full-size conductors is considered in the present work. The basis for this statistical approach is the comparison of the measured conductor critical current or current sharing temperature with the "potential" performance estimated from the strand data.

*This work, supported by the European Communities under the contracts of association between EURATOM and CRPP, was carried out within the framework of the European Fusion Development Agreement. The views and opinions expressed herein do not necessarily reflect those of the European Commission. The technical support of the Paul Scherrer Institute PSI is greatly acknowledged.
#rainer.wesche@psi.ch

CONDUCTOR PROPERTIES

NbTi Cable-in-Conduit Conductors

The main properties of the considered sub- and full-size conductors, used for the comparison of NbTi strand and CIC conductor performances, are listed in Table 1. A more detailed description of the conductors can be found in [2] and [3]. In the full-size conductors, the two conductor legs are connected by a bottom joint close to the high field region. A single SULTAN full-size sample, consisting of two different conductor legs, allows us to test two different conductors of similar performance in a single measurement campaign. In the sub-size conductors, the bottom joint is replaced by a U-bend leading to a hairpin sample.

Table 1: Main Properties of the NbTi CIC Conductors

CICC	Strand/Coating	Cabling Pattern	N_{NbTi}
NbTi #1	A/Ni	(1 sc + 7 Cu)×3×4×4	48
NbTi #2	B/SnAg	(1 Cu + 6 sc)×3×4×4	288
NbTi #3	B/Ni	(1 Cu + 6 sc)×3×4×4	288
NbTi #4	B/Ni & wraps	(1 Cu + 6 sc)×3×4×4	288
NbTi #5	C/Ni	(1 Cu + 6 sc)×3×4×4	288
PFIS L	D/Ni & wraps	(3×4×4×5)×6	1440
PFIS R	D/Ni	(3×4×4×5)×6	1440
LCJ	D/Ni	(1 Cu + 9 sc)×4×4×6	864

Nb_3Sn Sub-Size Cable-in-Conduit Conductors

For seven Nb_3Sn sub-size conductors, the strand and CIC conductor performances have been compared. The strand type and the conductor dimensions are listed in Table 2. Further conductor properties are gathered in Table 3. The hairpin conductors VAC-T and VAC-B were both fabricated of VAC Nb_3Sn strands left over from the fabrication of the Central Solenoid Model Coil (CSMC). The two conductors are distinguished by the cabling pattern. VAC-T is a triplet-based conductor, whereas VAC-B is a braided conductor. A more detailed description of the conductors can be found in [4]. The dipole pre-prototype conductor (DIPP) was manufactured of OST strands with non-copper critical current densities of 1100 A/mm^2 at 12 T and 4.2 K (electric field criterion of 0.1 μV/cm) [5].

Table 2: Dimensions of Nb_3Sn Sub-Size CIC Conductors

CICC	Strand	Dimensions (mm)
VAC-T	VAC CSMC	14.5 Jacket / 12.5 Cable
VAC-B	VAC CSMC	14.52 Jacket / 12.52 Cable
DIPP	OST1	18.4 × 7.7 Jacket 16.4 × 5.7 Cable
PITSAM 1	OST dipole	21.1 × 9.5 Jacket 17.9 × 6.3 Cable
PITSAM 2	OST dipole	12.6 × 12.6 Jacket 9.1 × 9.1 Cable
PITSAM 3	OST dipole	15.4 × 10.5 Jacket 11.9 × 7.0 Cable
PITSAM 5	OST dipole	12.57 × 12.57 Jacket 9.1 × 9.1 Cable

A special feature of the PITSAM 5 conductor is the change of the pitches in the region of the U-bend. This means that the pitches are short in the left leg, while they are long in the right leg.

Table 3: Cable Pattern and Twist Pitches of the Nb_3Sn Sub-Size CIC Conductors

CICC	Cable Pattern	N_{sc}	Twist Pitch (mm)
VAC-T	3×3×4×4	144	51/76/136/167
VAC-B	29 (braid) × 5	145	167
DIPP	3×3×3×4 (24 Cu)	84	58/95/139/213
PITSAM 1	3×3×4×4	144	58/95/139/213
PITSAM 2	3×3×3×4 (60 Cu)	48	58/95/139/213
PITSAM 3	3×3×3×4 (60 Cu)	48	58/95/139/213
PITSAM 5	3×3×3×4 (60 Cu)	48	34/95/139/213 83/140/192/213

Nb_3Sn Full-Size Cable-in-Conduit Conductors

In the case of 14 Nb_3Sn full-size conductors a complete characterisation of the strands is available. The main properties of the seven full-size SULTAN samples are gathered in Table 4. The SULTAN samples TFAS 1 and TFAS 2 are of Toroidal Field Model Coil (TFMC) type [6], [7]. The cable pattern of these conductors is 3×3×5×4×6. In the conductors TFAS 1 EAS and TFAS 2 OCSI all 1080 strands are superconducting, whereas in TFAS 1 OST2 and TFAS 2 OKSC each first stage triplet consists of 2 Nb_3Sn strands and one copper wire, i.e. 720 Nb_3Sn strands and 360 Cu wires. All other full-size Nb_3Sn CIC conductors are of ITER type (see also [8]). The cabling pattern of the ITER conductors is {(2 Nb_3Sn + 1 Cu) × 3 × 5 × (5 + core)} × 6, where the cores consist of 3 × 4 copper wires. Thus, the number of Nb_3Sn strands is 900, while the number of copper wires is 522. In the TFPRO 2 OST2 conductor, the pitches of the first stages were significantly enlarged.

Table 4: Main Properties of Nb_3Sn SULTAN Full-Size Samples (L Left Leg, R Right Leg)

CICC Strand L/R	Dimensions (Jacket) (mm)	Twist Pitch (mm)
TFAS 1 EAS/OST2	40.4/37.2	45/87/126/166/415
TFAS 2 OCSI/OKSC	40.4/37.2	45/87/126/166/415
TFPRO 1 EAS/EAS	L 43.45/40.25 R 42.05/38.85	45/87/126/245/460
TFPRO 2 OST2/OST1	L 41.45/38.25 R 42.05/38.85	116/182/245/415/440 45/87/126/245/460
JATF 1 Mitsubishi/Hitachi	43.9/40.6	45/85/130/250/450
JATF 2 Hitachi/Mitsubishi	42.7/39.3	45/85/130/250/450
KOTF KAT/KAT	L 43.7/40.5 R 43.7/39.9	42/80/125/240/450

STRAND PROPERTIES

NbTi Strands

The temperature and field dependencies of the non-Cu critical current density of all NbTi strands have been described by the following scaling law [9]

$$J_c(B,T) = \left(\frac{C_0}{B}\right)\left(1-t^{1.7}\right)^{\gamma} b^{p}\left(1-b\right)^{q} \qquad (1)$$

where $t = T/T_c$, $b = B/B_{c2}(T)$, T_c the critical temperature and B_{c2} the upper critical field.

$$B_{c2}(T) = B_{c20}\left(1-t^{1.7}\right) \qquad (2)$$

The properties of the NbTi strands and the corresponding scaling parameters are gathered in Table 5.

Table 5: NbTi Strand Scaling Parameters

Strand	A	B	C	D
d (mm)	0.87	0.70	0.70	0.73
Cu:non-Cu	1.12	1.05	7.5	1.41
p	1.55	1.65	1.4	1.92
q	1.85	1.80	1.55	2.03
γ	1.79	1.88	1.90	2.22
C_0 (kA T/mm^2)	286	271	181	477
T_c (K)	8.79	8.74	8.95	9.02
B_{c20} (T)	16.00	15.89	15.48	14.90

Nb_3Sn Strands

There exist several scaling relations to describe the field, temperature and strain dependencies of the critical current density of Nb_3Sn strands. In the present work, for all Nb_3Sn strands except the Korean KAT strand the Twente [10], [11] and the Durham scaling relations [12] have been used.

In order to define the strand scaling parameters, the Twente and the Durham scaling relations are briefly described. The Twente scaling relations can be written as

$$I_c(B,T,\varepsilon) = \frac{C_1}{B}\cdot s(\varepsilon)\cdot\left(1-t^{1.52}\right)\cdot \left(1-t^2\right)\cdot b^{0.5}\cdot(1-b)^2 \quad (3)$$

with

$$t = \frac{T}{T_c^{\,*}(\varepsilon)} \qquad b = \frac{B}{B_{c2}^{\,*}(T,\varepsilon)} \quad (4)$$

$$B_{c2}^{\,*}(T,\varepsilon) \cong B_{c2m}^{\,*}(0)\cdot s(\varepsilon)\cdot\left(1-t^{1.52}\right) \quad (5)$$

$$T_c^{\,*}(\varepsilon) = T_{cm}^{\,*}(0)\cdot s(\varepsilon)^{1/3} \quad (6)$$

$$s(\varepsilon) = 1 + \frac{C_{a1}\left(\sqrt{\varepsilon_s^{\,2}+\varepsilon_{0,a}^{\,2}} - \sqrt{(\varepsilon-\varepsilon_s)^2+\varepsilon_{0,a}^{\,2}}\right) - C_{a2}\cdot\varepsilon}{1-C_{a1}\cdot\varepsilon_{0a}} \quad (7)$$

$$\varepsilon_s = \frac{C_{a2}\cdot\varepsilon_{0,a}}{\sqrt{C_{a1}^{\,2}-C_{a2}^{\,2}}} \quad (8)$$

$$\varepsilon = \varepsilon_a + \varepsilon_m \quad (9)$$

where B is the magnetic field, B_{c2}* the inhomogeneity averaged, effective upper critical field, B_{c2m}* the inhomogeneity averaged maximum upper critical field at $\varepsilon = 0$, T the temperature, T_c* the inhomogeneity averaged maximum critical temperature at $B = 0$, ε the strain, ε_a the applied axial strain, ε_m the thermal pre-compression strain, ε_s the axial difference between a three dimensional deviatoric strain minimum and the position of the maximum in axial strain sensitivity results and $\varepsilon_{0,a}$ the remaining strain component. Three superconducting parameters (C_1, B_{c2m}*(0), T_{cm}*) and four deformation related parameters (C_{a1}, C_{a2}, $\varepsilon_{0,a}$, ε_m) need to be determined by a least squares fit to the measured strand data. The scaling parameters for the EAS, OST2 and OST dipole strands are gathered in Table 6. The scaling parameters are based on measurements performed at the University of Twente.

Table 6: Nb_3Sn Strand Twente Scaling Parameters

Strand	**EAS**	**OST2**	**OST dip.**
C_{a1}	71.39	81.69	114.14
C_{a2}	28.28	35.25	82.75
$\varepsilon_{0,a}$ [%]	0.25	0.15	0.237
ε_m [%]	-0.12	-0.06	-0.11
B_{c2m}*(0) [T]	35.75	34.02	29.05
T_{cm}*(0) [K]	16.52	16.21	15.91
C_1 [A·T][a)]	12171 TFAS 12407 TFPRO	17790 TFAS 17624 TFPRO	49405

[a)] Adjusted to the results of the witness strand measurements.

The Durham scaling relations can be written as

$$J_e(B,T,\varepsilon) = A(\varepsilon)\cdot\left[T_c^{\,*}(\varepsilon)\cdot\left(1-t^2\right)\right]^2 \left[B_{c2}^{\,*}(T,\varepsilon)\right]^{n^*-3} b^{p-1}(1-b)^q \quad (10)$$

with

$$B_{c2}^{\,*}(T,\varepsilon) = B_{c2}^{\,*}(0,\varepsilon)\cdot\left(1-t^{\nu}\right) \quad (11)$$

$$\left(\frac{A(\varepsilon)}{A(0)}\right)^{w/u} = \left(\frac{T_c^{\,*}(\varepsilon)}{T_c^{\,*}(0)}\right)^{w} = \frac{B_{c2}^{\,*}(0,\varepsilon)}{B_{c2}^{\,*}(0,0)} = 1 + c_2\cdot\varepsilon^2 + c_3\cdot\varepsilon^3 + c_4\cdot\varepsilon^4 \quad (12)$$

where J_e is the engineering critical current density, $b = B/B_{c2}$*(T,ε) and $t = T/T_c$*(ε). The scaling parameters for the VAC CSMC [13], OST1, OCSI, OKSC, Mitsubishi and Hitachi strands are gathered in Table 7.

Table 7: Nb_3Sn Strand Durham Scaling Parameters

Strand	**VAC**	**OST1**	**OCSI**
p	0.4625	0.9631	0.8869
q	1.452	2.229	2.174
n*	2.457	2.532	2.500
ν	1.225	1.518	1.500
w	2.216	2.423	2.200
u	0.051	0.1155	0
$A(0)$ [$Am^{-2}T^{3-n^*}K^{-2}$] [a)]	1.004×10^7	4.32×10^7	2.87×10^7
T_c*(0) [K]	17.58	16.71	17.50
B_{c2}*(0,0) [T]	29.59	29.72	28.47
c_2	-0.6602	-0.7816	-0.7392
c_3	-0.4656	-0.6318	-0.5071
c_4	-0.1075	-0.1732	-0.0838

Table 7: Nb_3Sn Strand Durham Scaling Parameters (continued)

Strand	OKSC	Hitachi	Mitsubishi
p	0.4556	0.6231	0.4422
q	1.723	1.9221	2.064
n^*	2.642	2.5203	2.7756
ν	1.318	1.52	1.52
w	2.43	1.8195	1.6132
u	-0.811	-0.6282	-0.9198
$A(0)$ [$Am^{-2}T^{3-n^*}K^{-2}$]	1.26×10^{7} a)	4.30×10^{7}	2.17×10^{7}
$T_c^*(0)$ [K]	17.22	17.26	17.10
$B_{c2}^*(0,0)$ [T]	29.41	29.46	28.21
c_2	-1.0768	-0.6462	-0.889
c_3	-1.1514	-0.4536	-0.9423
c_4	-0.4125	-0.09534	-0.3503

a) Adjusted to the results of the witness strand measurements.

The VAC CSMC, OST1, OCSI and OKSC strands were characterised at Durham University. The strand scaling parameters of the Mitsubishi and Hitachi strands were provided by the Japanese ITER team.

COMPARISON OF CABLE AND STRAND PROPERTIES

The variation of the magnetic field within a SULTAN sample of circular shape is to a first approximation

$$B(r) = B_b + \frac{\mu_0 I}{2\pi r_c}\left(\frac{r}{r_c} + \frac{r_c}{R-r}\right) \qquad (13)$$

where I is the operating current of the CIC conductor, μ_0 is the permeability of free space, r_c is the radius of the cable space, R is the distance of the two conductor legs and r is a coordinate perpendicular to the background field B_b generated by the SULTAN facility. For simplicity, it is assumed that the field contours remain parallel to the background field. In the case of rectangular conductors, the maximum and the minimum fields in the central plane of the conductor have been calculated numerically. It is supposed that the field varies linearly between these two values within the conductor cross-section. Due to the twist pitch, the strands cycle in and out of the high field region. The average electric field is calculated under the assumption that in a sufficiently long CIC conductor (i.e. longer than one cable pitch) each strand is found with the same probability at any position of the cable cross-section. In addition, a uniform current distribution among insulated strands is considered, i.e. no inter-strand current sharing is allowed. The resulting average electric field for a circular CIC conductor without central channel is

$$\frac{E_{av}}{E_c} = 2\int_{-r_c}^{+r_c} \frac{\left(r_c^{\,2} - r^2\right)^{1/2}}{\pi r_c^{\,2}} \left(\frac{J}{J_c(B,T,\varepsilon)}\right)^n dr \qquad (14)$$

where J is the non-copper operation current density and E_c = 0.1 μV cm^{-1}. In our calculations, the integral was replaced by a summation with a step width of 0.01 r_c. The conductor temperature within the cross-section is supposed to be constant. Furthermore, the difference between the conductor and helium temperature has been neglected in the comparison with the experimental data. By definition, the cable critical current density is reached when the calculated average electric field, E_{av}, equals E_c. In the case of full-size conductors with a central channel [14] or of rectangular conductors, it is necessary to adjust Eq. (14) to the geometry in question.

RESULTS

NbTi CIC Conductors

The measured and the calculated "potential" current sharing temperatures of NbTi sub-size cable-in-conduit conductors are compared in Fig. 1. The measured current sharing temperatures of all considered NbTi sub-size cable-in-conduit conductors are close to the "potential" values. The deviations from the "potential" values are typically of the order of 0.1 K. In the case of the conductors NbTi #2 and #3, the current sharing temperature was also measured after cyclic loading. The cyclic loading was performed by charging the conductor for 1400-times with a current of 40 kA in a background field of 5 T generated by the SULTAN facility. In both conductors, the current sharing temperatures, measured before and after cyclic loading, are not significantly different. This result reflects the fact that NbTi strands are not very sensitive to mechanical damage.

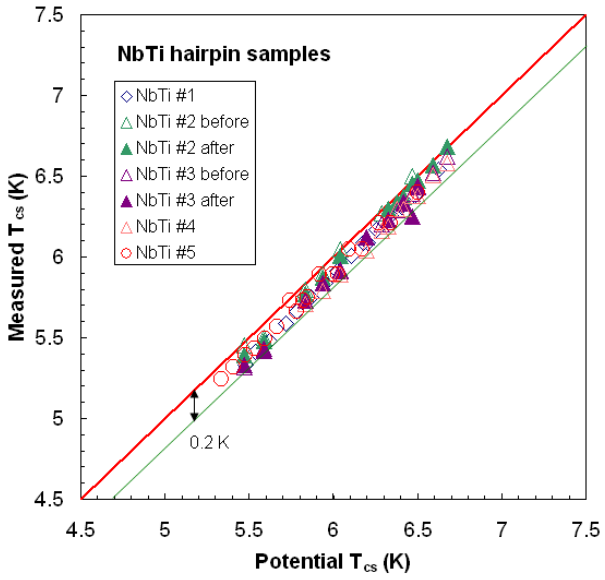

Figure 1: Measured versus "potential" current sharing temperature for NbTi hairpin (sub-size) CIC conductors.

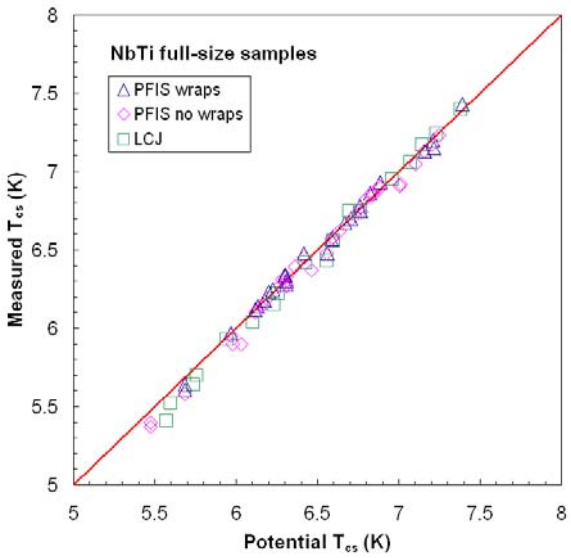

Figure 2: Measured versus "potential" current sharing temperature for NbTi full-size CIC conductors.

The ac losses, measured after cyclic loading, were considerably lower than those found before cyclic loading [2]. The observed change in the ac losses is the consequence of an increased transverse resistance between adjacent strands. The absence of a change of the critical current and the current sharing temperature of NbTi #2 and #3 after cyclic loading suggests that the current distribution among the strands is not significantly altered.

In Fig. 2, the measured current sharing temperatures of full-size NbTi conductors are shown as a function of the "potential" values. The agreement of measured and "potential" values is even better than in the case of the sub-size conductors. The deviations from the potential values are typically less than 0.1 K.

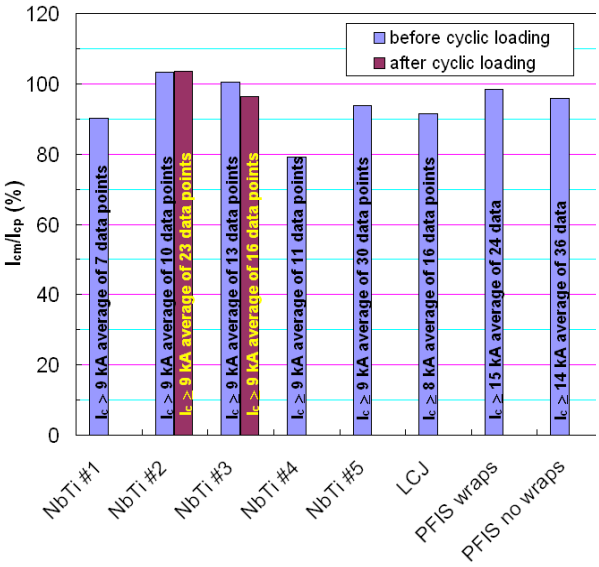

Figure 3: Ratio of measured to "potential" critical current for NbTi sub- and full-size CIC conductors.

In Fig. 3, the ratios of the measured to the "potential" critical current are shown for both the sub- and full-size NbTi CIC conductors. For seven out of eight conductors, this ratio exceeds 90%. Again the effects of cyclic loading on the performance of the two tested conductors NbTi #2 and #3 are negligible. In one of the sub-size conductors (NbTi #4), characterised by Ni coating of the strands and the presence of sub-cable wraps, the ratio of measured to "potential" critical current reaches only ≈80%.

The deviations of measured and "potential" values include the errors of the temperature measurements of the SULTAN sample, the uncertainties in the strand scaling relation and deviations from the assumed uniform current distribution. Before the mounting of the temperature sensors was improved at the end of the year 2006 the accuracy of the measurement of the conductor temperature was approximately ±0.05 K. In the case of NbTi #3, this accuracy of the temperature measurement leads to an uncertainty of ±10% in the cable critical current at a field of 6 T and a temperature of 6 K. In the measurement of the critical current of Strand B, the accuracy of the temperature measurement was about ±0.02 K, which is equivalent to an error bar of ±5% for the strand critical current at 6 T and 6 K. The scaling relation for the strand critical current tends to underestimate I_c below 6 T, whereas it overestimates I_c above 6 T in the case of Strand B. The errors related to strand scaling parameters are in the range of interest typically less than 8%. Moreover, the assumption that each strand is found with the same probability at any position of the cable cross-section is not exactly correct for the relatively short lengths of conductor in high field in a SULTAN test. Based on these considerations, we can conclude that cable critical currents, which exceed 90% of the "potential" values, suggest that in the conductor in question the current carrying capacity of the superconducting strands is fully used.

Nb_3Sn Sub-Size CIC Conductors

The comparison of cable and strand performances is more complex in the case of Nb_3Sn conductors. The upper critical field and the transition temperature of Nb_3Sn depend on the strain state of the superconductor. As a consequence, the critical current is a function of temperature, field and strain. In general, the strain state of the Nb_3Sn in a CIC conductor is different from that in a single strand measurement for example on a Ti6Al14V ITER barrel. As long as the strain does not exceed a critical value the critical current depends reversibly on this parameter. Application of a strain exceeding the critical value leads to micro-crack formation in the brittle Nb_3Sn filaments. The irreversible reduction of the critical current is reflected by the fact that the critical current, measured after unloading, is lower than the initial I_c value found before any loading. The estimation of a "potential" cable critical current suffers from the not exactly known strain state of the Nb_3Sn strands in a cable-in-conduit conductor.

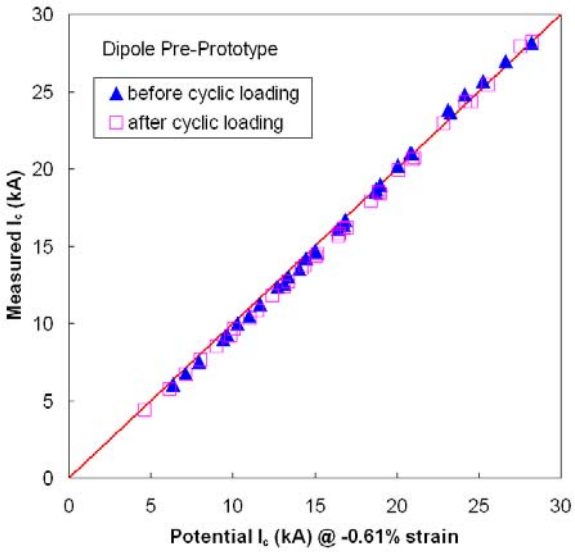

Figure 4: Measured critical current of the dipole pre-prototype (DIPP) conductor as a function of the "potential" values.

First, the results of two Nb_3Sn sub-size conductors of rectangular cross-section, which show a very good DC performance, are presented. In Fig. 4, the measured critical currents of the dipole pre-prototype (DIPP) conductor [5] are shown as a function of the "potential" critical currents. The calculation of the "potential" critical current is based on a strain of -0.61%. This value seems to be reasonable for a CIC conductor with stainless steel conduit. Due to the differences in the coefficients of thermal expansion of stainless steel and the Nb_3Sn strands the cool-down from the reaction temperature for the formation of Nb_3Sn (≈650°C) to 4.2 K leads to a compressive strain in the strands, while the jacket experiences a tensile strain.

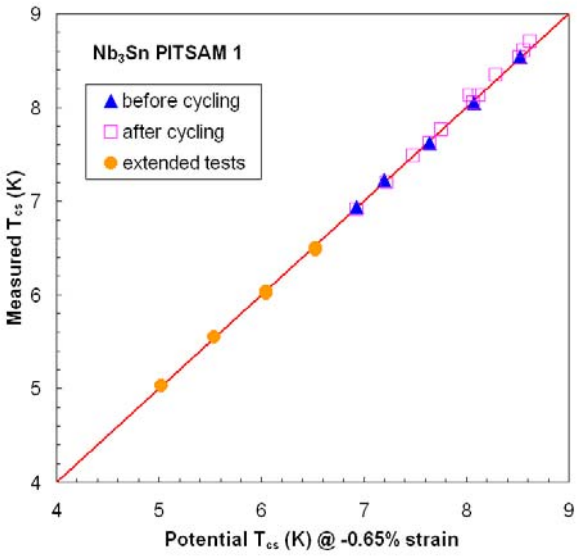

Figure 5: Measured T_{cs} values of the PITSAM 1 conductor as a function of the "potential" values.

The agreement of the measured and the "potential" critical current is excellent, as illustrated in Fig. 4. Moreover, 1000 load cycles at a current of 22 kA in a background field of 9 T were found to have a negligible effect on the critical current of the DIPP conductor. The DC performance of the DIPP conductor can be well described by not degraded strands and a single strain value of -0.61%. In contrast to the results for the CSMC model coil [15], [16], it is not necessary to introduce a load-dependent extra strain ($\varepsilon_{extra} \propto \mathbf{I}\times\mathbf{B}$) to describe the data.

In Fig. 5, the current sharing temperature (T_{cs}), measured in the PITSAM 1 conductor [17] is compared to the "potential" values. To obtain a good agreement of measured and "potential" values it was necessary to enhance the strain to -0.65%. The results of the PITSAM 1 conductor are consistent with not degraded strands and a strain of -0.65%. Again the whole data set can be described by a single value of strain, which is independent of the transverse load. Furthermore, the T_{cs} values measured after 1000 load cycles at 21 kA in a field of 11 T are not significantly different from those found before cyclic loading. The absence of cyclic load degradation is a further hint that the strands in this conductor are not degraded. In the further considerations, we will use a strain of -0.65% as a reference value for the calculation of the "potential" I_c and T_{cs} values.

Two other hairpin Nb_3Sn CIC conductors were fabricated of VAC strands left over from the fabrication of the CSMC. One of these conductors is braided, whereas the other is triplet-based [4]. In Fig. 6, the measured current sharing temperatures are compared with the "potential" values, which are based on a strain of -0.65%. The T_{cs} values of the braided conductor are closer to the

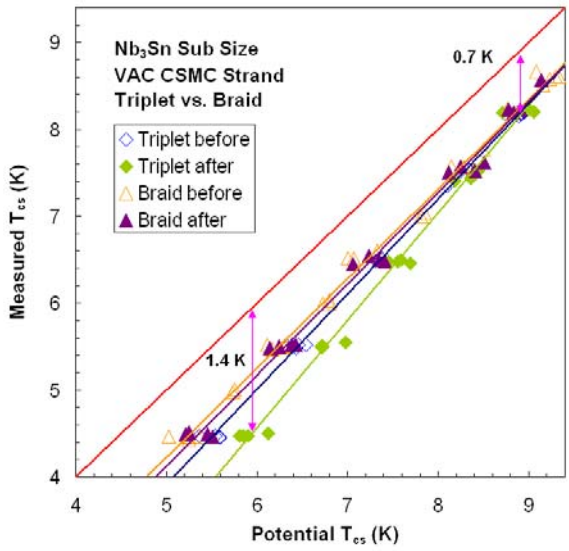

Figure 6: Measured versus "potential" T_{cs} values of the VAC-B and VAC-T conductors. The performance of the braided conductor (VAC-B) is closer to the "potential" values than that of the triplet-based conductor.

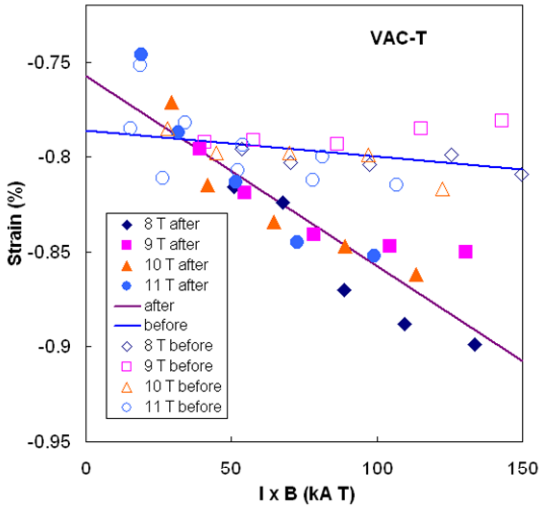

Figure 7: Strain values required to get a matching of cable and strand performances.

"potential" values than those of the triplet-based conductor. Moreover, the effect of cyclic loading on the T_{cs} of VAC-B is relatively small. The data, measured in the magnetic field range of 8 to 11 T, scatter around the trend lines. Especially for the triplet-based conductor VAC-T the difference of measured and "potential" T_{cs} increases with decreasing temperatures after cyclic loading, i.e. is larger at high I_c values. In principle, a matching of the cable T_{cs} values with the strand data can be always obtained by adjusting of the strain value for individual data points. The values of strain, obtained for the VAC-T conductor before and after cyclic loading are shown in Fig. 7. The results seem to indicate that the strain depends to a first approximation linearly on the transverse load. Nevertheless, the evolution of the performance of the conductor performance with cyclic loading suggests that the conductor is irreversibly degraded due to micro-crack formation in the Nb_3Sn filaments.

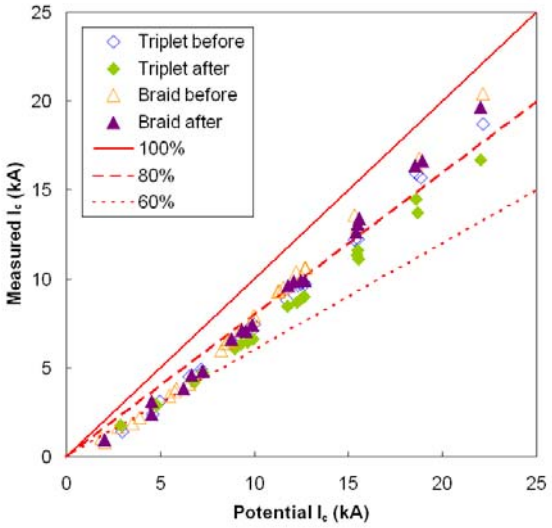

Figure 8: Measured versus "potential" I_c for the triplet- and braid-based conductors VAC-T and VAC-B.

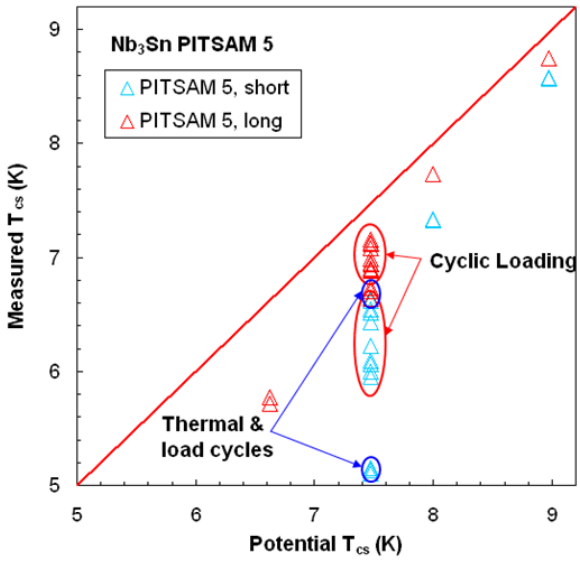

Figure 9: Comparison of the T_{cs} values, measured in the two legs of different pitch, with the "potential" T_{cs} values for a strain of -0.65%.

In Fig. 8, the measured critical current is shown as function of the "potential" values for a single strain value of -0.65%. Considering critical currents well above 10 kA, we find that the critical currents of the braided conductor, measured before and after cyclic loading, are close to 90% of the "potential" critical current. For VAC-T, the critical currents, measured before cyclic loading, reach approximately 85% of the "potential" values. After 1000 load cycles the critical current is reduced to ≈75% of the "potential" values.

In the case of the PITSAM 5 conductor, the pitch was changed in the region of the U-bend. Therefore, the twist pitch is short in the left conductor leg, whereas it is long in the right leg. In Fig. 9, the performances of the two conductor legs are compared to the "potential" T_{cs} values for a strain of -0.65%. The current sharing temperatures of the leg with longer pitches are higher than those of the leg with short pitches. In both conductors, T_{cs} decreases with cyclic loading (800 load cycles at 17 kA in a field of 8 T). However, the reduction is much more pronounced for the leg with the short pitches. After 800 load cycles the conductor is warmed up to room temperature and again cooled down to ≈4.5 K. After the thermal cycle and also after 100 additional load cycles the current sharing temperature was measured again at 17 kA in a field of 8 T. The "potential" T_{cs} is around 7.5 K. The reduction of T_{cs} due to the thermal cycle is much larger for the leg with short pitches. Thus, the measurement of T_{cs} at 9 T and 17 kA was only possible in the leg with long pitches (see data at "potential" T_{cs} of ≈6.6 K).

A summary of the performance of the considered Nb_3Sn sub-size CIC conductors after cyclic loading is presented in Fig. 10. The measured critical current is again compared with the "potential" values for a strain of -0.65%. The pre-prototype conductor (DIPP) and PITSAM 1 clearly reach the "potential" values.

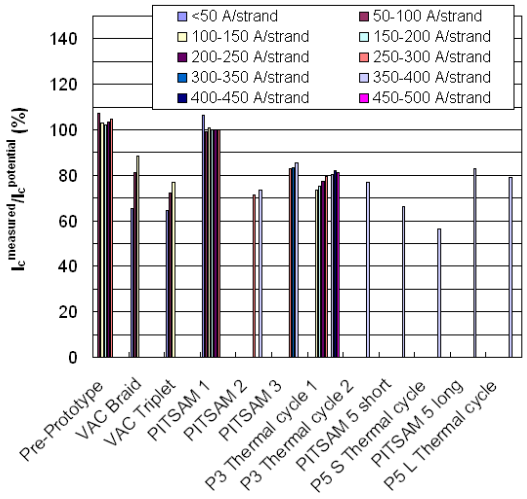

Figure 10: Comparison of the I_c values of various sub-size conductors, measured after cyclic loading, with the "potential" critical current. For some of the conductors, the effect of thermal cycles is also illustrated.

For VAC braid (VAC-B), PITSAM 3 and PITSAM 5 with long pitches, the critical current reaches ≈80% of the potential values. VAC-T, PITSAM 2 and PITSAM 5 with short pitches reach approximately 70% of the "potential" critical current after cyclic loading. A moderate effect of thermal cycles was observed for PITSAM 3 and PITSAM 5 with the long pitches. In PITSAM 5 with short pitches a pronounced reduction of the critical current was found after a single thermal cycle. Conductors of rectangular shape (DIPP, PITSAM 1 & 3) seem to be less sensitive to degradation than round (VAC-T) or square conductors (PITSAM 2 & 5). Longer pitches were also found to be advantageous (PITSAM 5 long).

Nb_3Sn Full-Size CIC Conductors

In a first campaign two European SULTAN samples TFAS 1 (EAS and OST legs) and TFAS 2 (OCSI and OKSC legs) were tested. The cabling pattern of these conductors is of TFMC-type. In the other full-size conductors the cabling pattern is that envisaged to be used for the ITER TF conductors.

In Fig. 11, the measured T_{cs} values of the four TFAS conductors are compared with the "potential" values for a strain of -0.65%. For the TFAS-OST conductor, the initial T_{cs} values are well above the "potential" values, suggesting that the strain in this conductor is considerably smaller than -0.65%. The trend lines for the TFAS-OST conductor indicate that the T_{cs} at 50 kA after cyclic loading is 1 K lower than the initial value. The TFAS-EAS and OKSC conductors show a less pronounced performance loss with cyclic loading. The TFAS-OCSI conductor was found to be relatively insensitive to cyclic load degradation in spite of the fact that the initial T_{cs} values are well below the "potential" current sharing temperatures.

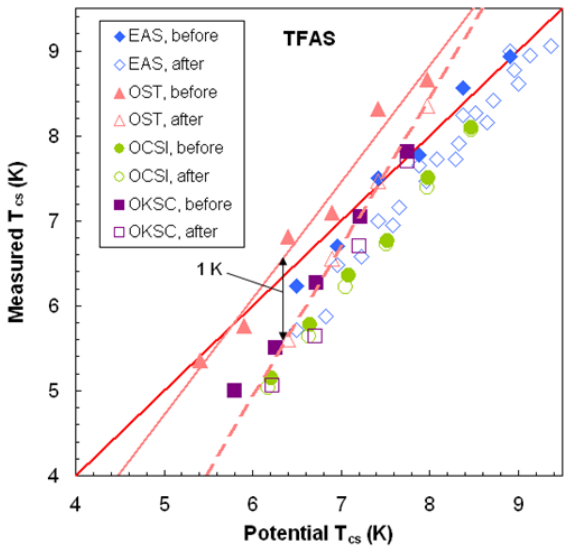

Figure 11: Comparison of the T_{cs} values of the four TFAS conductors, measured before and after cyclic loading, with the "potential" values for a strain of -0.65%.

In Fig. 12, the measured T_{cs} values of the two EAS legs of TFPRO 1 are plotted as a function of the potential values. The two legs are only distinguished by slightly different void fractions (EAS1: 33.8%, EAS2: 29.2%) [8]. Most of the measured data points of both conductors are slightly above the "potential" T_{cs} values suggesting that the strain in these two conductors is slightly lower than -0.65%. The data suggest that the performance of the EAS2 leg is slightly better than that of the EAS1 leg. Nevertheless, the strand current carrying capacity is practically fully used in both conductor legs. In addition, we found no evidence for cyclic load degradation.

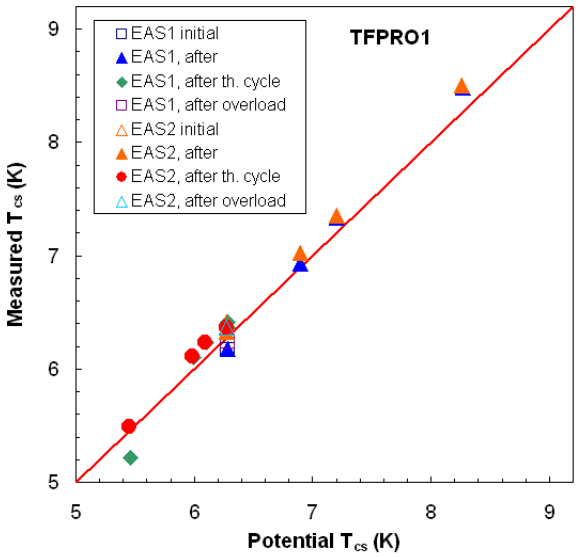

Figure 12: Measured T_{cs} values of TFPRO 1 EAS1 and EAS2 legs versus the "potential" values.

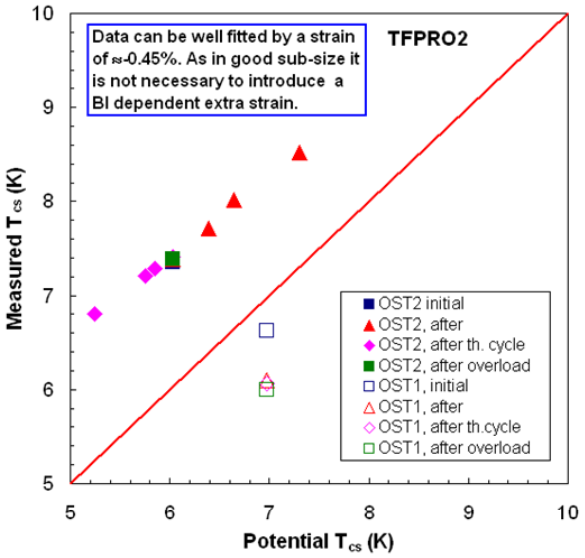

Figure 13: Measured T_{cs} values of TFPRO 2 OST1 and OST2 legs versus the "potential" values. The data for OST2 are consistent with not degraded strands and a strain around -0.45%.

The measured T_{cs} values of TFPRO 2 OST2 are well above the "potential" values for a strain of -0.65%, as illustrated in Fig. 13. The data are consistent with not degraded strands and a single strain value of ≈-0.45% independent of the transverse load. No performance evolution with cyclic loading was observed. On the other hand, the OST1 leg shows T_{cs} values below the "potential" values. Moreover, the T_{cs} after cyclic loading is significantly reduced.

For various full-size CIC conductors, the ratios of the measured to the "potential" critical current after cyclic loading are presented in Fig. 14. Especially for the TFAS conductors this ratio depends on current.

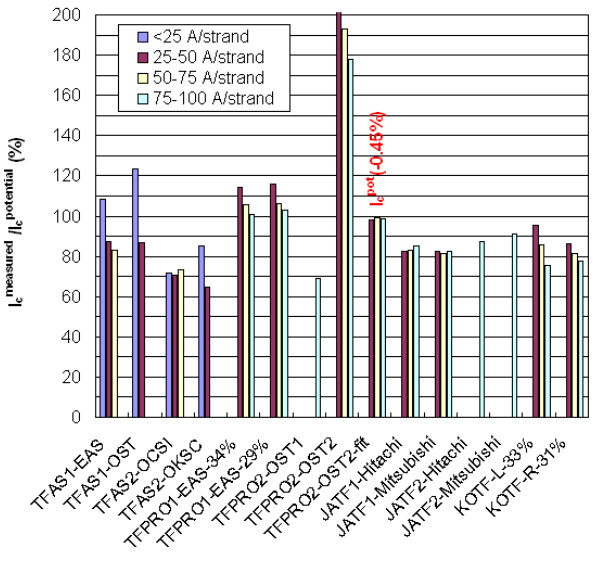

Figure 14: Performance summary of various full-size CIC conductors.

In the case of the TFAS conductors with strongly current-dependent ratios of measured to "potential" critical current the data can be well described by a combination of reduced strain values and a reduced effective superconductor cross-section [6]. The reduced cross-section seems to originate from micro-crack formation in the Nb_3Sn filaments. Considering currents of more than 75 A per strand the potential critical current has been achieved in the TFPRO2 OST2 and the TFPRO1 EAS1 & 2 conductors. The Japanese conductors JATF1 & 2, fabricated of Mitsubishi and Hitachi strands, reach 83 to 91% of the "potential" values. In the two legs of the Korean SULTAN sample KOTF 75 to 78% of the "potential" critical current has been achieved. The ratio of measured to "potential" I_c is below 70% for the TFPRO 2 OST1 conductor.

CONCLUSION

The measured critical current of NbTi full- and sub-size CIC conductors reaches typically more than 90% of the "potential" values. Only in the sub-size conductor NbTi #4 this ratio is ≈80%. The deviation of the measured current sharing temperatures from the potential values is typically less than 0.1 K. In addition, the two conductors NbTi #2 & #3, exposed to cyclic loading, did not show any degradation. These results suggest that a current non-uniformity originating from the resistance distribution in the joints does not severely degrade the performance of the SULTAN NbTi samples.

In the case of two sub-size Nb_3Sn conductors (DIPP, PITSAM 1), the measured T_{cs} values reach the "potential" values for strain values of -0.61% (DIPP) and -0.65% (PITSAM 1). Both conductors have been found to be insensitive to cyclic load degradation. A further aspect of importance is the fact that the complete data sets of these two conductors can be well described by a single value of strain independent of the transverse load, i.e. the value of **I×B**. In other conductors, the initial T_{cs} values were found to be well below the "potential" values for a strain of -0.65%. Typically these conductors show also a performance reduction with cyclic loading or after thermal cycles.

The current sharing temperatures of the TFAS full-size CIC conductors [6] were found to be significantly below the "potential" values. Moreover, pronounced cyclic load degradation was found in the TFAS 1 OST conductor. A first series of ITER-type conductors showed an improved performance. In the TFPRO 1 EAS conductors, the measured T_{cs} values were close to the "potential" values and cyclic load degradation is absent. The TFPRO 2 OST2 conductor showed excellent performance, however, the strain seems be much smaller than -0.65%. The data suggest that the real strain is as low as ≈-0.45% in this conductor. This single strain value provides a good description of the whole data set independent of actual transverse load. The extra strain needed to describe the behaviour of some conductors may therefore simply reflect that some damage is present in these conductors.

Especially the TFPRO 2 OST1 conductor showed a performance well below the "potential" values. Furthermore, the current sharing temperature declined with cyclic loading. Despite of performances that are much better in the ITER-type conductors than in the TFAS conductors, there remain doubts if in all ITER conductors the current carrying capacity of the strands is fully used.

REFERENCES

[1] P. Bruzzone, A. Anghel, A. Fuchs, G. Pasztor, B. Stepanov, M. Vogel, G. Vecsey, IEEE Trans. Appl. Supercond. 12 (2002) 520.
doi: 10.1109/TASC.2002.1018457

[2] R. Wesche, A. Anghel, B. Stepanov, M. Vogel, P. Bruzzone, Cryogenics 45 (2005) 755.
doi: 10.1016/j.cryogenics.2005.10.002

[3] R. Wesche, B. Stepanov, P. Bruzzone, IEEE Trans. Appl. Supercond. 16 (2006) 819.
doi: 10.1109/TASC.2006.871274

[4] P. Bruzzone, B. Stepanov, R. Wesche, Advances in Cryogenic Engineering (Materials) 52 (2006) 558.

[5] P. Bruzzone, B. Stepanov, R. Wesche, A. Portone, E: Salpietro, A. Vostner, A. della Corte, IEEE Trans. Appl. Supercond. 16 (2006) 894.
doi: 10.1109/TASC.2006.873320

[6] P. Bruzzone, M. Bagnasco, D. Ciacynski, A. della Corte, A. Di Zenobio, R. Herzog, Y. Ilyin, B. Lacroix, L. Muzzi, A. Nijhuis, B. Renard, E. Salpietro, L.S. Richard, B. Stepanov, S. Turtù, A. Vostner, R. Wesche, L. Zani, R. Zanino, IEEE Trans. Appl. Supercond. 17 (2007) 1370.
doi: 10.1109/TASC.2007.898504

[7] D. Ciazynski, Fus. Eng. Des. 82 (2007) 488.
doi: 10.1016/j.fusengdes.2007.01.024

[8] P. Bruzzone, B. Stepanov, R. Wesche, E. Salpietro, A. Vostner, K. Okuno, T. Isono, Y. Takahashi, H.C. Kim, K. Kim, A.K. Shikov, V.E. Sytnikov, IEEE Trans. Appl. Supercond. 18 (2008) 459.
doi: 10.1109/TASC.2008.922266

[9] L Bottura, IEEE Trans. Appl. Supercond. 10 (2000) 1054.
doi: 10.1109/77.828413

[10] A. Godeke 2005, Performance boundaries in Nb_3Sn superconductors, PhD thesis, University of Twente, ISBN 90-365-2224-2.

[11] A. Godeke, B. ten Haken, H.HJ. ten Kate, D.C. Larbalestier, Supercond. Sci. Technol. 19 (2006) R100.
doi: 10.1088/0953-2048/19/10/R02

[12] D.M. Taylor, D.P. Hampshire, Supercond. Sci. Technol. 18 (2005) 2041.
doi: 10.1088/0953-2048/18/12/005

[13] D.M.J. Taylor, D.P. Hampshire, *Test of advanced Nb_3Sn strands*, Durham University, Final report EFDA03-1126 2003.

[14] R. Wesche, R. Herzog, P. Bruzzone, Supercond. Sci. Technol. 21 (2008) 054001.
doi: 10.1088/0953-2048/21/5/054001

[15] R. Zanino, N. Mitchell, L. Savoldi Richard, Cryogenics 43 (2003) 179.
doi: 10.1016/S0011-2275(03)00035-3

[16] N. Mitchell, Fus. Eng. Des. 66-68 (2003) 971.
doi: 10.1016/S0920-3796(03)00237-0

[17] A. Vostner, P. Bauer, R. Wesche, U. Besi Vetrella, B. Stepanov, A. della Corte, A. Portone, E. Salpietro, IEEE Trans. Appl. Supercond. 18 (2008) 544.
doi: 10.1109/TASC.2008.921329